This is a post-peer-review, pre-copyedit version of an article published in Experiments in Fluids. The final authenticated version is available online at: https://doi.org/10.1007/s00348-020-2911-2

Measurement of Nuclei Seeding in Hydrodynamic Test Facilities.

Patrick S. Russell · Luka Barbaca · James A. Venning · Bryce W. Pearce · Paul A. Brandner

Abstract

Microbubble populations within the test section of a variable pressure water tunnel have been characterised for various operating conditions. The tunnel was operated with demineralised water and artificially seeded with microbubbles from an array of generators located in a plenum upstream of the tunnel contraction. The generators produce a polydisperse population of microbubbles 10–200 µm in the diameter. The microbubbles are generated from supersaturated feed water within a confined turbulent cavitating microjet. The generator and tunnel operating parameters were systematically varied to map the range of nuclei concentrations and size ranges possible in the test section. Microbubbles were measured with Mie-Scattering Imaging (MSI), an interferometric sizing technique. A new method was introduced to calibrate the detection volume and extend the dynamic range of the MSI. The acquisition and processing of microbubble measurements with MSI have a fast turn-around such that nuclei concentration measurements are approaching real-time. Estimation of the total bubble concentration was within 5% of the sampled concentration after only 100 detections but 10^4 were necessary for full histogram convergence. The tunnel is operated with water at low dissolved gas content to ensure all injected microbubbles dissolve and do not complete the tunnel circuit. As a result of this the injected population is altered by dissolution as well as pressure change during the short residence between plenum and test section. The transformation is shown to be complex, changing with tunnel operating conditions. The measured test section nuclei populations were found to follow a power law for the higher concentrations. Test section nuclei concentrations of 0–24 mL^{-1} can be achieved through variation of generator and tunnel operating parameters.

P. Russell
University of Tasmania
E-mail: patrick.russell@utas.edu.au

Graphic abstract

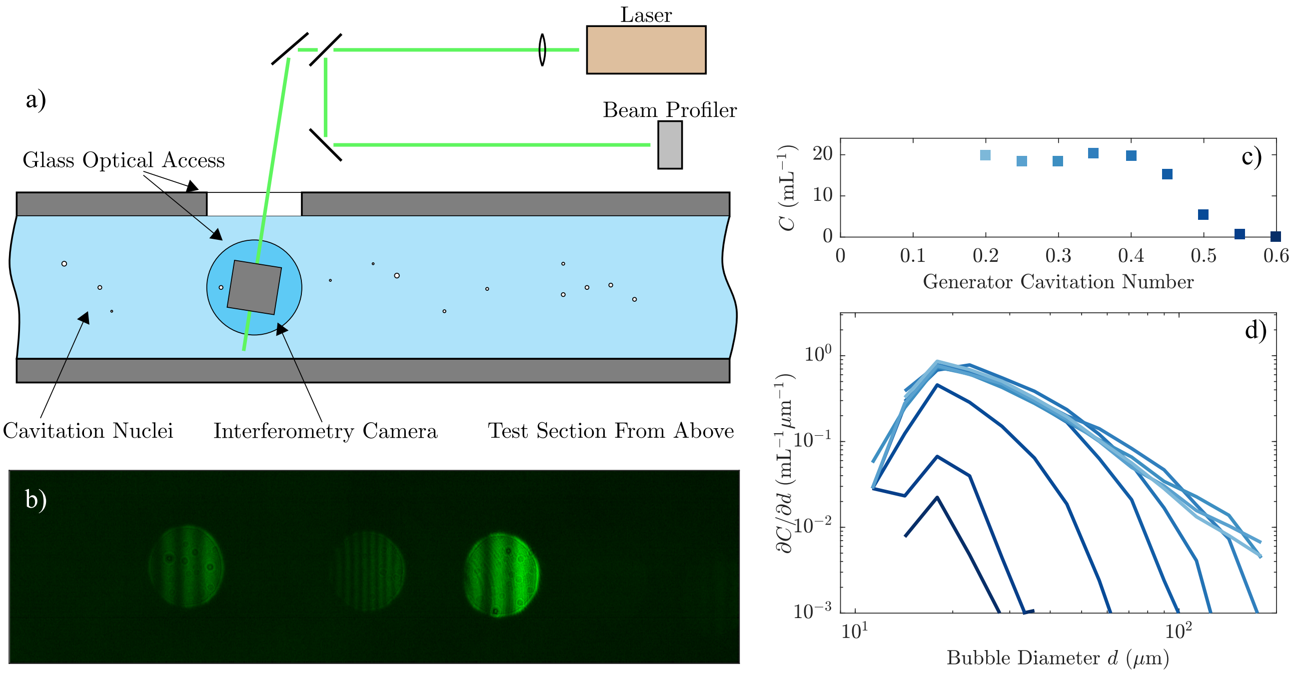

a) A schematic of the experiment. b) Sample image data. c) Measured concentration of the seeded microbubble cavitation nuclei. d) Distribution of bubble concentration by size.

1 Introduction

Microbubble disperse flows are intrinsic to surface oceanography and naval hydrodynamics as they control, or interact with, many phenomena and processes of interest including cavitation inception and dynamics, gaseous diffusion, noise generation, acoustic and shockwave propagation and turbulence. With regard to cavitation, microbubbles provide nuclei that control the inception and dynamics of unsteady cavitation; but cavitation itself is also a prolific source of microbubbles by its very nature. Modelling of these flows experimentally remains a challenge as microbubble concentrations and size ranges may vary over several orders of magnitude. To this end, several techniques for generating and measuring microbubbles have been developed in the Cavitation Research Laboratory (CRL) at the Australian Maritime College (AMC) (Brandner, 2018). Sample results from these techniques for measuring microbubbles or nuclei populations in the AMC cavitation tunnel are shown in Fig. 1. Overall concentrations and sizes range over 10 and 5 orders of magnitude respectively. The population with the largest concentrations and sizes is typical of that in the wake of a cavitating object at relatively high Reynolds numbers (Russell et al., 2018). This population of high concentration/larger microbubbles has been measured using Long-range Microscopic Shadowgraphy (LMS). The most sparse population shown in Fig. 1 is typical of the background or naturally occurring nuclei population ever present in the AMC cavitation tunnel under normal operating conditions. These nuclei cannot be measured using optical techniques due to their small sizes and low concentrations. These have been measured via mechanical activation using a Cavitation Susceptibility Meter (CSM) (Khoo et al., 2017). The intermediate population is representative of a test flow artificially seeded with a modest concentration of microbubbles in the size range 2 to 200 µm for experimental modelling of cavitation inception. It is the characterisation of these intermediate populations within cavitation tunnels that is the subject of the present work.

The measurement of micro-bubble concentrations on-the-order-of 0-1 cm^{-3} with in-focus imaging is challenging, as discussed in a review paper on optical measurement techniques in fluid flows by Tropea (2011). In order to accurately size the bubbles, high magnification is required (field-of-view ~ 1 mm^2), resulting in the need for an impractically large number of images to observe enough detections for a converged measurement. To circumvent this issue interferometric techniques possessing a larger detection volume have been employed.

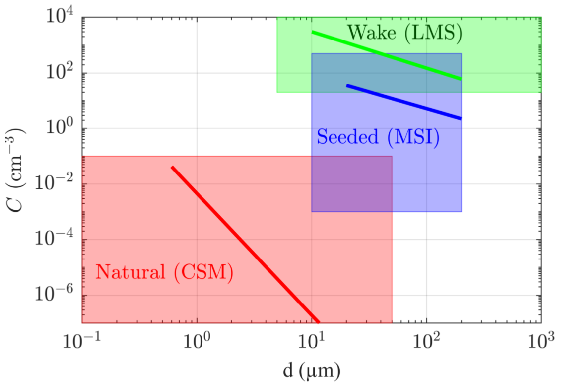

Fig. 1 Nuclei distribution graph showing the bubble diameter, d, and concentration, C, ranges (shaded regions) for which practical measurements can be made using the Cavitation Susceptibility Meter (CSM), Mie Scattering Imaging (MSI) and Long-range Microscopic Shadowgraphy (LMS). Optical methods (e.g. IMI and LMS) are more suitable for higher concentrations of larger bubbles, while mechanical activation (CSM) is suitable for lower concentrations of smaller bubbles. The lines represent recent nuclei measurements at the AMC cavitation tunnel.

Early use of interferometric sizing techniques was reported for application in particle spray measurements, particularly in fuels (König et al., 1986; Skippon and Tagaki, 1996; Mounaïm-Rousselle and Pajot, 1999), and its development stemmed from the Global Phase-Doppler technique (Albrecht et al., 2013). Various implementations of the method have been developed, but the fundamental operating principle is the same, monochromatic light illuminates a bubble (or particle) and the scattered light produces an interference pattern. Information from the interference pattern is used to determine the bubble/particle size. Based on the slight differences between implementations, the method has been given different names; Interferometric Laser Imaging, Mie Scattering Imaging, Global Phase Doppler, Inteferometric Laser Imaging for Droplet Sizing, Interferometric Particle Imaging, and Interferometric Mie Imaging. We adopt the nomenclature of Graßmann and Peters (2004) and label the method Mie Scattering Imaging (MSI). This name reflects the techniques roots in the mathematically rigourous scattering of a plane wave by a sphere, postulated by Lorentz-Mie Theory (Bohren and Huffman, 2008).

Numerous extensions to MSI technique have been proposed in the published literature. A cylindrical lens can be incorporated to compress interference patterns in one dimension on imaging sensors (Masanobu et al., 2000; Kobayashi et al., 2000; Qieni et al., 2014). This reduces overlap of the fringes when multiple bubbles (or particles) are present and thus increases the concentration limit of the technique. The use of laser light also lends itself to simultaneous particle-image velocimetry and size measurement (Kawaguchi and Maeda, 2005). Novel methods have also been proposed to measure the 3D location of droplets in addition to the diameter through an optical arrangement that shears the interference pattern as the distance from the sensing plane increases (Brunel and Shen, 2013; Shen et al., 2013). Alternatively the size of the interference disc can also be used to estimate the out-of-plane location (Tropea, 2011).

Comparative experimental measurements of nuclei size distributions using MSI and various other nuclei measurement techniques have shown large discrepancies in the results (Quérel et al., 2010; Ebert et al., 2015; Boucheron et al., 2018; Birvalski and van Rijsbergen, 2018). In order to minimize the uncertainty and errors in the results obtained using MSI, Lacagnina et al. (2011) suggest that a systematic calibration of the method has to be performed. The most detailed treatment of sensitivity and uncertainty analysis has been reported by Dehaeck and van Beeck (2007). They identify measurement of the lens and sensor plane location as potential a source of error and uncertainty in calibration experiments. Custom lenses or specialist optics knowledge can provide the required precision (Mées et al., 2010), but for a standard multi-element lens and camera such data may not be accessible. Dehaeck and van Beeck (2007) examined multiple methods for calibration and full experimental calibration is identified as very accurate. A calibration experiment of a similar nature was conducted by Russell et al. (2019). Individual microbubbles from a mono-disperse bubble generator were simultaneously recorded using shadowgraphy and MSI. A calibration procedure was demonstrated and using this method measurements with the two techniques deviated by less than ±0.5µm for bubbles 40-150µm in diameter. In addition, the calibration method for the size dependent measurement volume proposed by Ebert (2015) was extended. The method of Ebert (2015) assumes was developed from Laser-Doppler Velocimetry theory (Albrecht et al., 2013) and assumes a Gaussian beam profile (Ebert et al., 2016), whereas the procedure of Russell et al. (2019) avoids this assumption through measuring the beam profile directly. The efficacy of the method was demonstrated using the location of the bubbles in the beam measured from the shadowgraphy data. The details of this correction are critical, as just like shadowgraphy, the measurement volume of MSI changes with bubble size (Mées et al., 2010). Due to its sensitivity, volumetric correction errors may then account for some of the discrepancies between the microbubble measurement techniques reported in hydrodynamic test facilities (Lacagnina et al., 2011; Mées et al., 2010; Ebert et al., 2015).

The ability to measure and precisely control nuclei populations in water tunnels enables rigorous comparison of results from different facilities (Lindgren, 1966). The natural population present in each facility is in equilibrium with the dissolved gas content, and often nuclei control is achieved solely through dissolution of these populations by degassing the water (Liu et al., 1993; Etter et al., 2005; Weitendorf et al., 1987). However, natural populations may still be partly comprised of nuclei biological, and particulate in nature, the cavitation susceptibility of which cannot be measured optically. To produce populations of the desired concentration and strength that can be measured optically, the AMC water tunnel uses filtered, degassed water, to which artificial microbubble nuclei are injected using a seeding system (Brandner et al., 2006). This tunnel architecture emulates the French Grand Tunnel Hydrodynamique (GTH) (Lecoffre et al., 1987). This facility uses cavitating micro-jets of supersaturated water to generate the artificial microbubble nuclei. These nuclei generators were characterised outside the water tunnel and typically produce a poly-disperse plume of bubbles 2-200µm in diameter (Giosio et al., 2016). However, their response to changing tunnel operating conditions has not yet been fully characterised. The scope of the present work is to present the application of the refined MSI technique for nuclei measurement in hydrodynamic test facilities and analyse the effect of variable operating conditions to better understand the range of nuclei populations that can be tested for in the facility.

A short summary of the equations used for bubble sizing and antecedent Lorentz-Mie theory are presented in Sect. 2, including deliberation on the choice of measurement parameters. Experimental method and equipment, including an outline of data processing technique, are found in Sect. 3. Calibration methods are also presented in Sect. 3.2. This includes an improvement to the *in-situ* calibration of the measurement volume that extends the dynamic range of the technique. The measurement technique is used to characterise the range of microbubble sizes and concentrations that can be produced in the test section by the nuclei seeding system (Sect. 4). The modification of generated populations with changing tunnel conditions is shown to be complex, as the microbubble population generated upstream are affected by the change in pressure through the contraction, and dissolution that occurs due to bubble residence time. To explore this process a quasi-steady model of bubble dynamics with dissolution is used to simulate the modulation of the injected population (Sect. 5). Results of the simulation are then related to the observed population as tunnel conditions vary, and the implications for tunnel operation explored. Conclusions are presented in Sect. 6.

2 Mie Scattering Imaging

Theory and experiments have shown that a linear mapping can be constructed between the size of a microbubble ($\sim 1-100$ μm) and the number of interference fringes of light it scatters across a narrow angular domain (Mées et al., 2010; Boucheron et al., 2018). This can be expressed by equation

$$d = \frac{KN}{\alpha} \qquad \frac{[\mu\text{m}\ ^\circ]\ []}{[^\circ]}, \tag{1}$$

where d is the bubble diameter in microns, N the number of fringe wavelengths across the angle α, and K is a proportionality constant. K depends primarily on the wavelength of light used to illuminate the bubble and the scattering angle θ_s, which is defined as the angle between the camera, the bubble and the direction in which the light is propagating (Fig. 2 a). An example of interference pattern resulting from Mie scattering of a 94 um bubble (Russell et al., 2019) is presented in Fig. 2c, along with the calibrated shadowgraphy image of the same bubble captured simultaneously (Fig 2b). In order to create an image disc containing the frequency information, MSI images must be taken off-focus, as otherwise the scattered light would focus back to a point. In experiments by Russell et al. (2019), equation 1 was recast to map the wavelength of interference fringes in pixels, to the diameter of the bubble, by introducing a second constant A. Its value encapsulates the angle a single pixel represents in an interference pattern. By converting N/α to a wavelength (λ_{deg}), and substituting A, equation (1) becomes,

$$d = \frac{KN}{\alpha} \qquad \frac{[\mu\text{m}\ ^\circ]\ []}{[^\circ]} \tag{2a}$$

$$= \frac{K}{\lambda_{deg}} \qquad \frac{[\mu\text{m}\ ^\circ]}{[^\circ]} \tag{2b}$$

$$= \frac{K}{A\ \lambda_{px}} \qquad \frac{[\mu\text{m}\ ^\circ]}{[^\circ\ \text{px}^{-1}]\ [\text{px}]}. \tag{2c}$$

Light scattered by a bubble can be decomposed into two components. One parallel to the scattering plane, i.e. the plane containing the camera, bubble, and direction of propogation ($S_{||}$), and the other that is normal to the scattering plane ($S_{\perp}$). The intensity of each component is modulated by the angle between the polarisation of the laser and the scattering plane, called the polarisation angle ψ_s. Despite being overall less intense the $S_{||}$ component produces a more uniform fringe spacing making it preferred. For these experiments a scattering angle $\theta_\text{s} = 90^\circ$, with a polarisation angle $\psi_\text{s} = 90^\circ$ was used. A polarising filter on the lens admits only $S_{||}$ for measurement. Further discussion on the selection of these parameters is presented in Russell et al. (2019).

Calibration of the value for K can be determined by simulating intensity curves from theory and measuring the fringe wavelength for a range of bubble sizes. For 532 nm light where $\theta_\text{s} = 90^\circ$, K has been measured to be 39.8 μm·deg^{-1}. Experimental calibrations for the setup-dependent value A, and the size dependent measurement volume, are discussed in the following section.

3 Experimental Setup

Experiments were conducted in the Cavitation Research Laboratory (CRL) variable pressure water tunnel at the University of Tasmania. The test section is 0.6 m square by 2.6 m and operates with velocities of 2 to 13m/s and pressures of 4 to 400 kPa. To manage turbulence, upstream of the test section is a plenum containing a 6mm plastic honeycomb. The homogenised flow then passes through a contraction section leading to the test section entrance to constrict any remaining turbulence. The test section velocity is measured from the calibrated contraction differential pressure. Depending on the value, either high or low range Siemens Sitransp differential pressure transducers models 7MF4433-1DA02-2AB1-Z (pressure range 0-25 kPa) and 7MF4433-1FA02-2AB1-2AB1-Z (pressure range 0-160 kPa) are used, with estimated precision of the velocity measurements of 0.007 and 0.018 m/s respectively. The test section velocity has been measured to be spatially uniform to within 0.5%, and has temporal variations of less then 0.2%, with the free stream turbulence intensity of 0.5%. Further details of the facility are given in (Brandner et al., 2006, 2007; Doolan et al., 2013).

Nuclei injection was realized using an array of microbubble generators positioned in the plenum upstream of the tunnel honeycomb and contraction (Fig. 3). The generators operating principle is based on rapid expansion of supersaturated water in a confined turbulent jet. Supersaturated water is expanded through a ∅ 0.5 mm by 0.3 mm long orifice into a ∅ 1.2 mm by 200 mm long hypodermic tube, where micro-bubbles form in shear layer cavities. The generators produce poly-disperse plume of micro-bubbles 2-200 um in diameter (Giosio et al., 2016). The supersaturated water is created using a separate recirculating pressure vessel (saturation vessel) designed to facilitate the dissolution of gas into the liquid at high pressures and is capable of maintaining pressures of 100-20000 kPa.

The microbubble population generated is a function of the absolute and differential values of the saturation vessel (p_s) and tunnel plenum (p_p) pressures, where $\Delta p = p_s - p_p$. From which the dimensionless parameters including the Reynolds, Weber and cavitation numbers, and the saturation pressure ratio of the supply and tunnel water, may be formed. The Reynolds and Weber numbers are proportional to $\sqrt{\Delta p}$ and Δp respectively. The cavitation number and saturation pressure ratio may be defined as $p_p/\Delta p$ and p_s/p_p respectively. The first two parameters are relatively large and don't change appreciably for the range of pressures involved. The last two parameters arguably have the greatest effect on the generated population and hence ultimately the tunnel test section population. The cavitation number and saturation pressure ratio control the cavity and available gas volumes respectively. If it is assumed that the Reynolds and Weber numbers don't affect the flow then a series of pressure combinations can be set for which the cavitation number and saturation pressure ratio remain constant. However for each of these combinations Δp will change which controls the flow rate and hence the bubble production rate.

The array of generators can be configured to seed different areas of the tunnel cross section. Generators can be affixed in an 80 mm triangular grid pattern across the plenum. For the present study, three rows of 10 generators were used to seed a 300 mm high by 100 mm wide, nominally rectangular, area in the top half of the test section.

The MSI measurements were captured using a 48MP IO Industries Flare 48M30 CX high-speed CMOS camera equipped with a Sigma 180 mm 1:2.8 APO Macro DG-HSM lens, located above the test section. A Promaster HGX Prime 86 mm polarizing filter was attached to the lens. Bubbles were illuminated using an Ekspla NL204-SH TEM_{00} laser emitting 532 nm light with pulse frequency of up to 1kHz and the energy of 2 mJ per pulse. The beam was collimated using a planoconvex LA1978-A-ML coated lens with a focal length of 750 mm, and it was then passed through a Thorlabs BSF10-A 1" UVFS 10% Beam Sampler before being directed into the tunnel by a Thorlabs NB1-K12 1" Nd:YAG mirror. A schematic of the optical arrangement is shown in Fig. 4. Mirror M1 was mounted to a Melles Griot microstage to enable precise positioning and movement of the laser beam in the tunnel. The beam entered the tunnel test section horizontally through an 80 mm thick glass port, 145 mm below the test section ceiling. An angle of 87° to the port was chosen to prevent any reflected and refracted rays from overlapping the measurement beam. Accordingly, the camera was rotated so that the horizontal axis was parallel to the direction of beam propagation. The camera was set with the sensor-plane-normal perpendicular to the beam so that the measurement scattering angle was $\theta_s = 90°$ (Fig. 2a). The Ekspla laser was polarised horizontally giving an MSI polarisation angle $\psi_s = 90°$.

3.1 Processing

Images were analysed using a custom Matlab script. Each interference pattern was reduced to a representa-

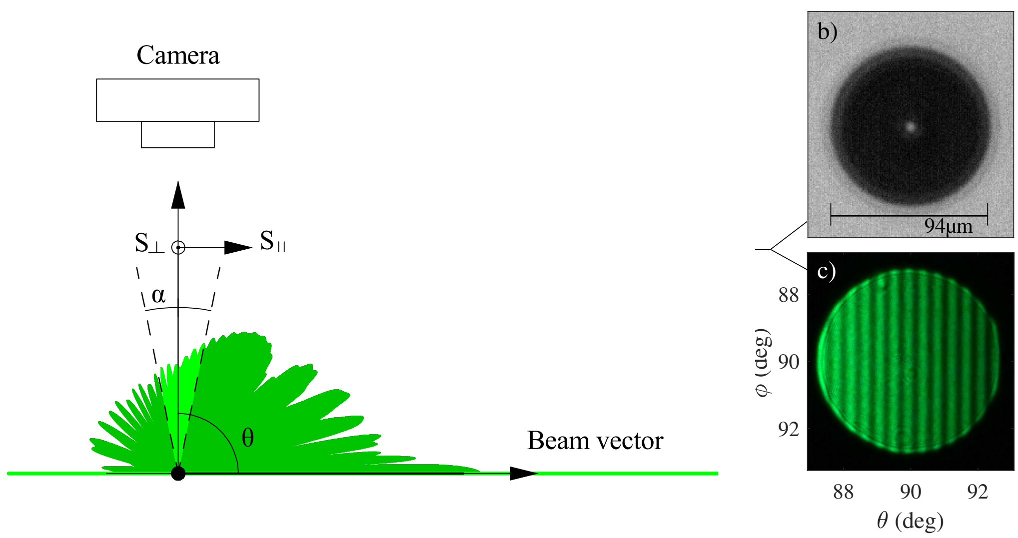

Fig. 2 a) A schematic of the MSI measurement technique. b) A shadowgraphy image of a 94 μm bubble. c) The interference pattern produced by the same bubble as in b).

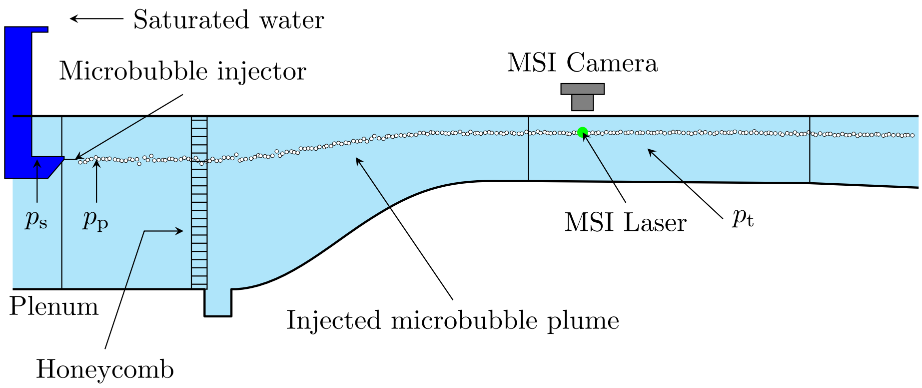

Fig. 3 A schematic of the tunnel seeding arrangement and measurement setup. Bubbles injected upstream of the honeycomb are advected into the test section. A horizontal laser beam across the test section is used to measure bubbles with MSI using a 90° scattering angle.

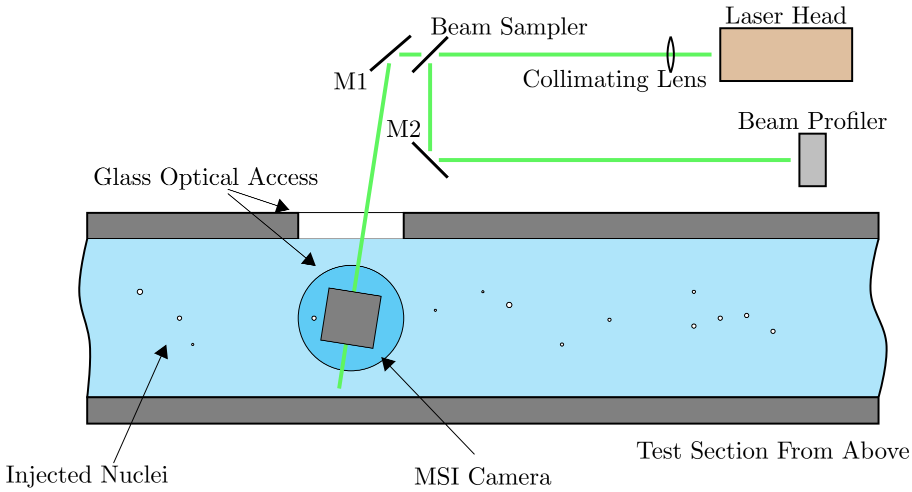

Fig. 4 An overview of the optical setup used to calibrate and capture the MSI images.

tive one-dimensional 'pixel series' of the same width as the original pattern. To generate these series, an iterative algorithm was used to extract the brightest interference pattern from an image, masking out the circular area afterwards. The masked image was then re-processed, and the processing continued until the median of the intensity series extracted in the current step was lower than a specified intensity threshold. Steps to locate and extract pixel series were,

1. Cross correlate a down-sampled image with a down-sampled template.
2. Locate correlation maximum.
3. Refine location by cross correlation in a limited domain with the full template.
4. Extract circular domain to generate an intensity series.
5. Sum each column of the extracted region and divide by the number of pixels to generate the 'pixel series'.
6. Mask out the region of the image and re-process the masked image.
7. If the median intensity of the pixel series is too weak, discard the last data and stop processing the image.
8. Filter and record all valid bubble locations and associated pixel series.

The last step filtered out bubbles that were too close together, or too close to the edge of an image, for the frequency detection algorithm to accurately measure the bubble size. In the case of two bubbles close together, both were discarded. This would cause an underestimate in the total bubble concentration if many bubbles overlapped, however, in present data such occurrence was rare, and it was observed no more than twice in 1000 detections. Once an image had been converted into a set of pixel series, auto-correlation was used to extract interference wavelengths. Each auto-correlation was refined by fitting a quadratic curve to the 7 points around the first maximum. The quadratic curve was then re-sampled with 1000 points to find the dominant wavelength in the interference pattern. The dominant wavelength was converted to bubble diameter through equation 2. The intensity of an interference pattern was defined as the 95th percentile of the extracted pixel series. This, along with the location of the bubble in the beam, was used to calculate the measurement volume of the technique for the optical setup described above.

3.2 Calibrations

To calibrate the magnification factor of images in the laser plane, mirror M1 (figure 4) was traversed in the stream-wise direction. The beam was moved 5 mm upstream and downstream of the initial position with the camera remaining fixed. Long exposure images capturing a large number of bubbles passing through the measurement volume were recorded. From these images, the average location of the center of the interference pattern was found, which represented the location of the center of the laser beam for each mirror position. By dividing the pixel shift in the image by the set mirror movement, the magnification factor expressed in px/mm was determined.

Calibration of the angular wavelength constant A was performed using the method described by Russell et al. (2019). A 0.5 mm thick masking plate with two holes was placed in between the lens and the beam at the glass-water interface. The holes were 6 mm in diameter, with the centers 14 mm apart. The plate was used to mask the interference pattern and produce a diffraction pattern from which the distance between the hole centers in pixels (D_{px}) could be measured. An example of the resulting image is shown in Fig. 5a. With the distance between the masking plate and the beam known, the angular constant A can be calculated from basic trigonometry as

$$A = \frac{2 \cdot \tan^{-1}\left(\frac{\text{Hole Distance}}{2\cdot\text{Beam Distance}}\right)}{D_{px}}. \tag{3}$$

A sample of 60 bubble instances was used to measure A, and to estimate the uncertainty. From Fig. 5b, $D_{\text{px}} =$ 260 px and has an estimated uncertainty of 10 pixels. D_{px} does not change appreciably across the measurement beam length. A was calculated to be $A = 0.0123\ \text{px} \cdot \text{deg}^{-1}$. Linearised uncertainty in d has been tabulated for a small and large bubble (Table 1), and overall uncertainty from this calibration remains a constant 3.85% from this source.

The effective measurement volume for MSI is dependent on bubble size and characteristics of the optical setup. The scattered light intensity of a bubble is nominally dependent on the square of the diameter. Therefore, for a Gaussian beam profile the scattered light intensity will depend on the bubble size and its location in the beam profile. Consequently, larger bubbles are measured across a wider area as less incoming light will be required to produce an interference pattern that is above the lower limit of camera sensitivity. However, a large bubble may also saturate the camera sensor so that the interference pattern cannot be discerned, so a portion at the center of the beam may have to be excluded. By using this approach, the dynamic range of the technique is optimised at the expense of more complex measurement volume calculation.

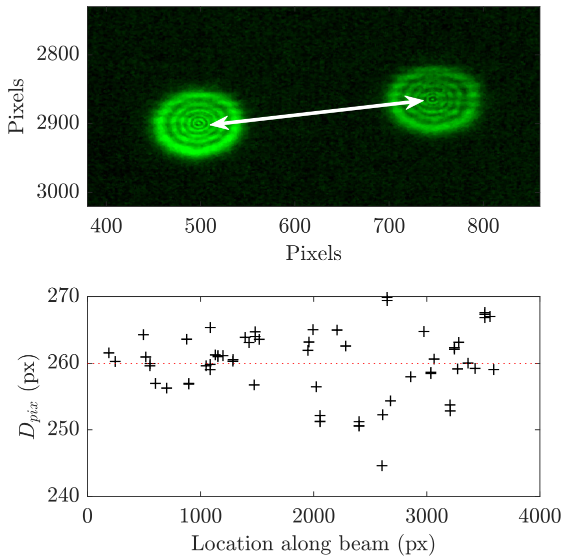

Fig. 5 a) An example of the two hole calibration pattern image obtained using a masking plate, from which D_{pix} is measured. b) A scatter of D_{pix} values across 60 bubble instances, with average value denoted with a dashed line.

Table 1 Tabulated values of the calculated diameter uncertainty due to a 10 pixel variation in A for a small and a large bubble.

Diameter (μm)	Uncertainty (μm)	Uncertainty %
20	±0.77	±3.85%
150	±5.77	±3.85%

To detail the volume correction calculation a camera-beam based coordinate system was introduced: the x-axis was placed along the beam center-line and the y-axis across one dimension of the beam profile, where both x and y were parallel to the focal plane of the camera. The z axis was normal to the focal plane of the camera.

As a bubble moves in the $x - y$ plane of the beam the centroid of the interference pattern shifts in the

MSI image. Pattern intensity depends on a bubble's y and z location in the beam profile. By plotting y position against measured intensity for a narrow size range, an estimate of the size-dependent maximum intensity at each y location with size was obtained (Fig. 6). For these data, bubbles were grouped into $d = \pm 2.5$ µm size bins and then sub-grouped into $y = \pm 0.5$ µm location bins. The 95$^{\text{th}}$ percentile of a single diameter/location bin was used to estimate the maximum intensity $I_{\max}(d, y)$ and is plotted with a red line in Fig. 6.

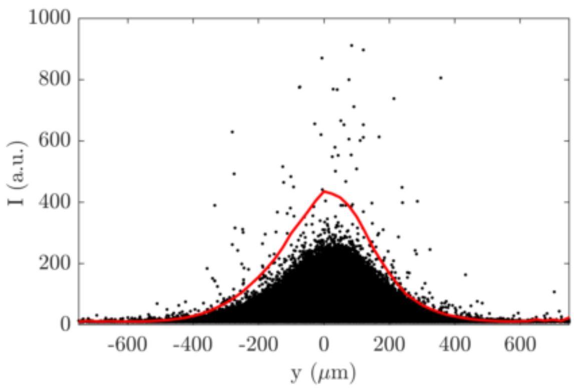

Fig. 6 A scatter of y-location and intensity of all bubble detections in 20-25 µm range ($\approx$ 30000 detections). A red line representing the 95th percentile calculated for 1 µm bins is plotted. This curve used to estimate the maximum intensity $I_{\max}(d, y)$.

As discussed by Ebert (2015), it is very unlikely that a bubble measurement is observed in the exact center of the beam for each size and y location, but with enough data the described process provides a reasonable estimate. By using all the data from an experimental campaign a large number of detections can be compiled. In the present experiment 2.46 million bubbles were detected. A minimum intensity threshold ($I_{min} = 50$) was applied to establish the maximum radius for effective measurement for each bubble size. A maximum intensity threshold $I_{max} = 400$ was also applied to ensure that bubble patterns too bright to be accurately sized were removed. This resulted with an annular area of effective measurement for some bubbles. In Fig. 7a the maximum intensity curve for two bubble size ranges, 20-25 µm and 80-85 µm, is plotted across the beam y-position. By plotting the intensity with colour, and stacking the intensity curves for each bubble size range horizontally, a contour plot showing the measurement area limits can be assembled, as show in (Fig. 7b). Multiplying the effective area by the measured beam length gives the effective measurement volume plotted against diameter in Fig. 7c. The comparatively low number of detections for bubbles $d > 150$ µm introduces scatter in the estimated measurement volume. A smoothing spline was used to calculate the final size dependent volume.

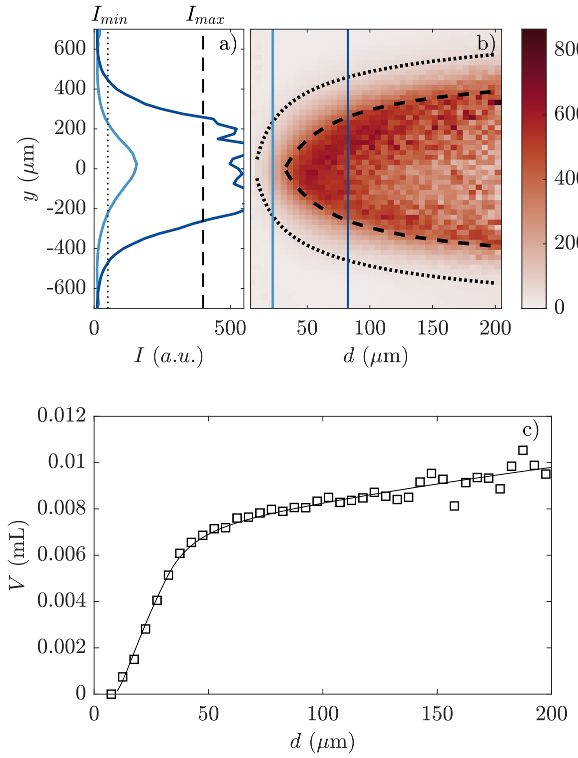

Fig. 7 a) The maximum intensity of interference patterns intensity for two bubble size ranges (d =20–25 µm and 80–85 µm) plotted against the vertical location of the bubble in the beam. b) A colourmap of the interference intensity mapped for a range of locations and measured diameters. The dotted contour is the minimum intensity threshold and the dashed line the maximum intensity threshold. The blue lines represent the data presented in a). c) The dependence of effective measurement volume on bubble size.

3.3 Convergence of concentrations and histograms

A study was performed to determine the number of bubble detections required to obtain a converged statistics for bubble size distribution. For this purpose a sample of 40000 detections was recorded. To calculate the total bubble concentration, the detection volume for each bubble was determined by interpolation of the fitted curve in Fig. 7c. The total bubble concentration was then calculated by

$$C = \left(\sum_{i=1}^{N_{bubbles}} \frac{1}{v_i} \right) / N_{images}, \tag{4}$$

where v_i is the size dependent measurement volume for the i^{th} bubble detection. To view these data as a distribution of bubble size, a histogram with logarithmic bin width was calculated. By dividing bin counts by the bin width, concentrations are expressed as $\frac{\partial C}{\partial d}$ at the bin centers. Integration between any two points on this curve estimates the concentration of bubbles within the sub-range. The total concentration was estimated using all 40000 detections. Total concentration was then iteratively calculated including one extra detection each time. Total concentration with each added bubble is plotted in Fig. 8a and the percent difference from the final estimate is plotted in Fig. 8b. The total concentration converges quickly so that a crude estimate to within 10% of the final concentration can be obtained with only 100 detections. To remain within 1% of the final estimated concentration 10000 detections are required. A similar number is required for convergence of the bubble size histogram with a bin size of 2 µm. This is presented visually in Fig. 9. A histogram was calculated with the addition of each bubble. Each histogram was normalised by its highest bin count. The normalised histogram was converted to colour and stacked horizontally. The distribution shape remained similar for $N > 10000$.

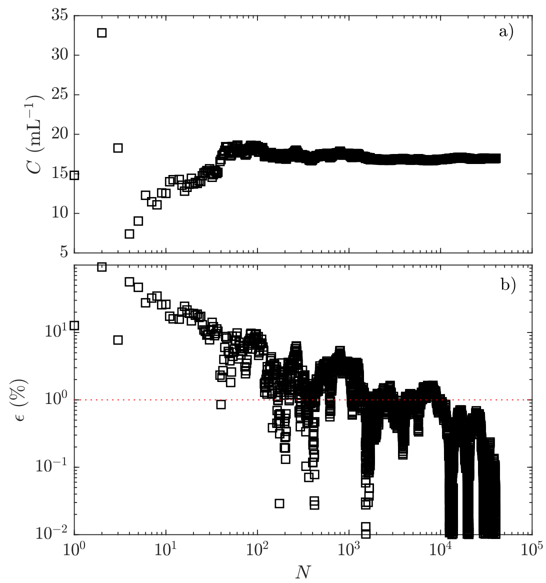

Fig. 8 a) Bubble total concentration (C) as a function of number of bubbles counted (N). b) Percent difference from the final concentration for large N. The difference is less than 1% which has been marked in red for $N > 10^4$.

An important consideration for implementation of MSI technique during the hydrodynamic facility operation is the time required to obtain the nuclei size

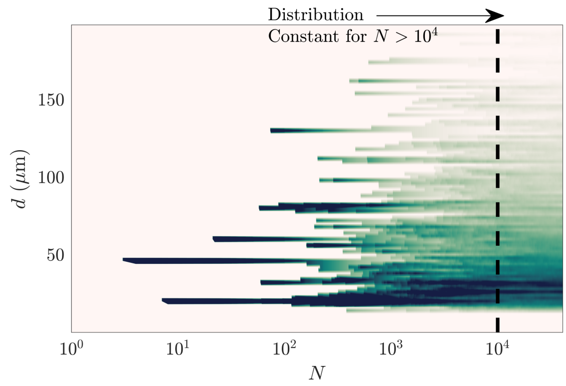

Fig. 9 Normalised histograms of the bubble distribution are oriented vertically and are presented as colour for an increasing number of bubble counts. The bin width is 2 µm. The population distribution converges for $N > 10^4$ detected bubbles for the presented bubble concentration.

distribution result. The time required to acquire and process images using the full camera sensor, as it was done for calibration and convergence analysis , while reasonable, still proved to be somewhat prohibitive during testing work-flow. In order to facilitate faster result turnaround, the images obtained for the analysis of the effect of tunnel operating conditions on the nuclei population were down sampled by the ratio of 2 in the direction of the fringe pattern. Additionally, the images were acquired over a reduced sensor area covering only the horizontal region illuminated by the laser beam. These steps yielded a measurement resolution of 4096 x 512 pixels. After applying these modification the time required to acquire a set of images needed for the converged result was in order of a few minutes, and therefore, the described MSI technique can be considered as a near real-time measurement. An example image captured by the measurement system is presented in Fig. 10.

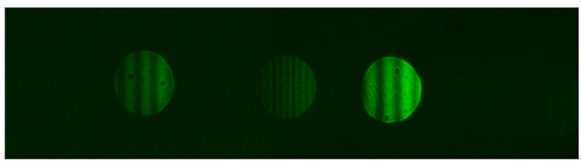

Fig. 10 An example image captured with MSI measurement system after a logarithmic intensity filter has been applied to enhance visibility of the interference patterns is presented. Bubble diameters observed in the image from left to right are 16 µm, 39 µm, and 14.5 µm respectively.

4 Tunnel Nuclei Results

4.1 Generator parameters

For constant tunnel operating conditions, the test-section nuclei content can be altered by varying nuclei generator parameters, namely the generator driving pressure Δp_{gen} and cavitation number σ_{gen}. In order to asses the influence of each of these parameters, bubble populations in the test-section were measured for a tunnel velocity of 7 m/s, while Δp_{gen} and σ_{gen} were varied independently of each other. Both generator parameters are coupled to tunnel operating conditions through the pressure in the plenum (p_p) where,

$$\Delta p_{gen} = p_s - p_p, \tag{5}$$

and

$$\sigma_{gen} = \frac{p_s - p_v}{p_s - p_p} = \frac{p_s - p_v}{\Delta p_{gen}}. \tag{6}$$

Therefore the tunnel pressure (p_t) was varied in conjunction with the saturation vessel pressure (p_s) to keep one generator parameter fixed while the other varied. Observations are made with the knowledge that tunnel pressure will influence dissolution processes. In Fig. 11a the total concentration of bubbles 10-200 µm in size are plotted for fixed Δp_{gen} = 400 kPa and varying σ_{gen}. Bubble concentration remains similar for $\sigma_{gen} \leq 0.41$, but decrease rapidly as σ_{gen} is further increased such that very few if any bubbles are measured for $\sigma_{gen} \geqslant 0.55$. Bubble size distributions for the data points shown in Fig. 11a are plotted in Fig. 11b. The distribution shape remains similar for low σ_{gen}, however a roll-off in the number of large bubbles produced can be observed. This roll-off shifts towards the smaller sizes as σ_{gen} increases. It is hypothesized that this trend would continue as σ_{gen} increases further, however this cannot be supported by experimental data as the roll-off moves below the minimum measured size. Irrespective of this, for $\sigma_{gen} > 0.55$ only a low concentration of very small bubbles remains.

In Fig. 12a the total bubble concentration is plotted for a constant $\sigma_{gen} = 0.25$, while the Δp_{gen} was varied. An increase can be observed in the total concentration with increasing Δp_{gen} , however C plateaus as Δp_{gen} increases above approximately 600 kPa. In contrast to the results for constant driving pressure the overall distribution shape remained identical Fig. 12b. The increase in concentration is mostly associated with the population of smaller bubbles, but the distributions suggest a more global increase in all bubble sizes is produced. This behaviour is consistent with the premise that for constant σ_{gen} the bubble production mechanism remains the same, but due to higher flow-rates through the generator the number of bubbles produced will increase. In both Fig. 11 and Fig. 12 the low number of detections introduces scatter into distributions for large bubble sizes. For the data in Fig. 11 and Fig. 12, the tunnel pressure is labelled with the additional horizontal axis above the graph. Note, that due to the contraction, at 7 m/s tunnel velocity, the pressure in the plenum will be $p_p = p_t + 35$ kPa.

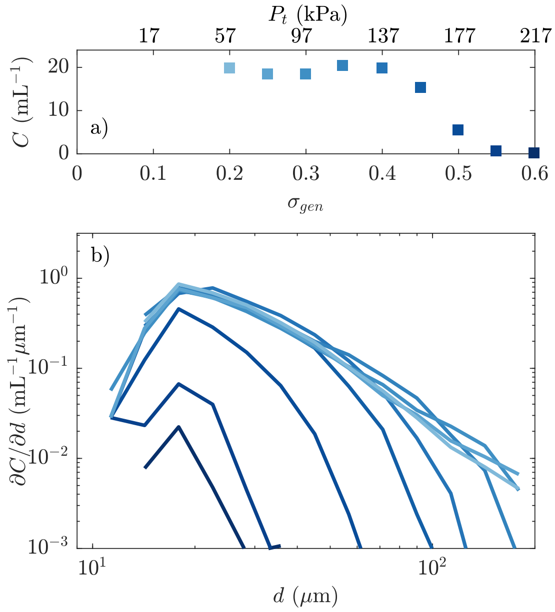

Fig. 11 a) Total bubble concentration plotted against σ_{inj}. The tunnel pressure was varied in conjunction with p_s to maintain constant driving pressure, Δp_{inj} = 400 kPa, with a constant tunnel velocity U_t = 7 m/s. b) A plot of size distributions for the examined range of σ_{inj}. For U_t = 7 m/s, pressure drop through the contraction leads to $p_p = p_t +$ 35 kPa.

The measurements of bubble population for varying σ_{gen} were performed for a range of driving pressures 100 kPa $\leq \Delta p_{gen} \leq$ 800 kPa, for tunnel velocity of 7 m/s. Resulting total bubble concentrations and size distributions are presented in Fig. 12. From the plot of total concentration (Fig. 13a), it can be seen that the critical cavitation number at which the concentration begins to reduce, increases with increasing driving pressure. In addition, the maximum concentration increases with increasing driving pressure. The distribution trends remain similar when comparing between driving pressures. It is observed that as the total bubble concentration increases the size distribution approaches a power law like behaviour. This power law distribution may be linked to the turbulent processes in the generator outlet, rather than the result of equilibrium processes on injected bubbles as they are advected through the plenum and contraction section. This is also true of distribution roll-off as dissolution processes in the tun-

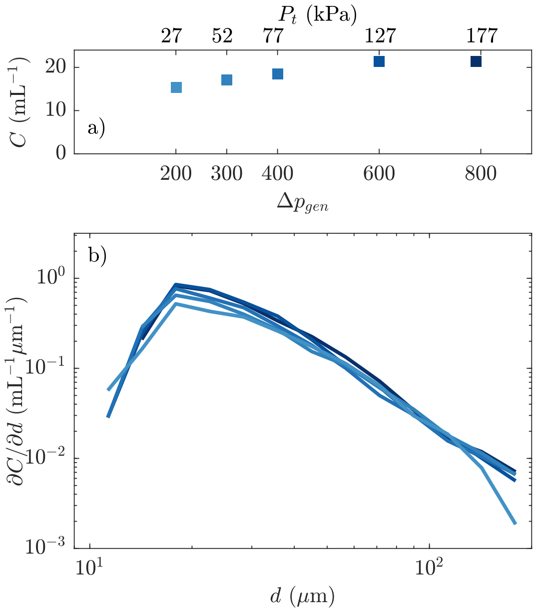

Fig. 12 a) Total bubble concentration plotted against Δp_{gen}. The tunnel pressure was varied in conjunction with p_s to maintain constant $\sigma_{gen} = 0.25$, with a constant tunnel velocity $U_t = 7$ m/s. b) A plot of size distributions for the examined range of Δp_{inj}. For $U_t = 7$ m/s, pressure drop through the contraction leads to $p_p = p_t + 35$ kPa.

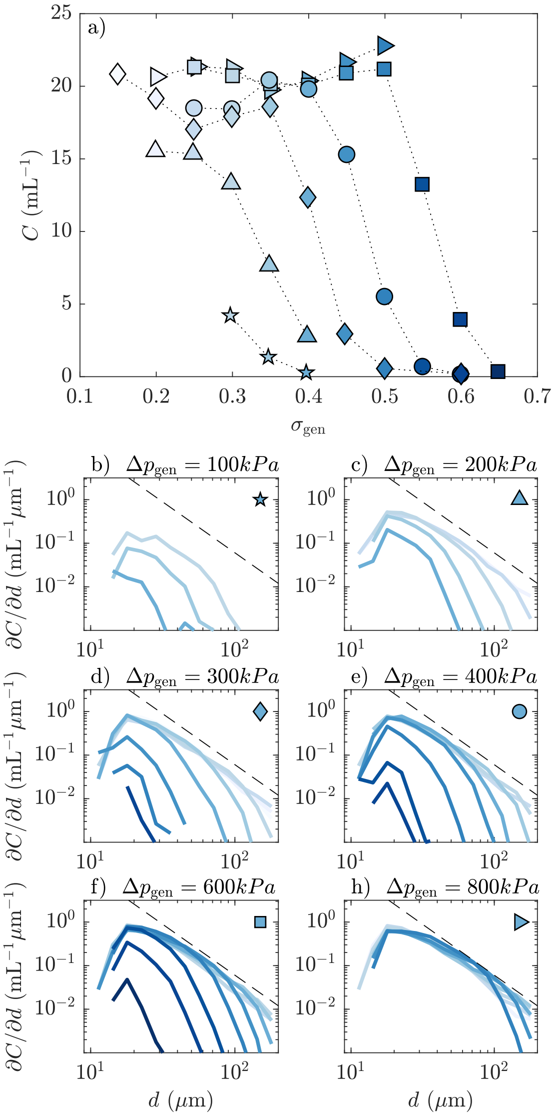

Fig. 13 a) Total concentrations plotted against σ_{gen} for various $\Delta_{P_{gen}}$. Each subplot (b-g) represents bubble size distributions for different σ_{gen} for a particular value of $\Delta_{p_{gen}}$. σ_{gen} is represented by the colour in each subplot that corresponds to the colours in a). The plots are for a fixed $U_t = 7$ m/s, while the dissolved oxygen content was in range 2.6 - 3.4 ppm. As a visual aid a curve denoting an approximate power law has been annotated on distribution plots.

nel are more likely to impact smaller bubbles due their increased surface area to volume ratio. The distributions move closer to the annotated power law across Fig. 13b-g as the driving pressure increases. This is the manifestation of the increase in total concentration with increasing driving pressure

4.2 Dissolved Oxygen Content

As previously mentioned the tunnel is designed to operate with a dissolved oxygen content (DO_2) of 30% of saturation concentration at atmospheric pressure, to ensure that all injected microbubbles dissolve and do not complete the tunnel circuit. Low DO_2 content promotes dissolution of the generated microbubble populations between the point of injection and measurement location in the tunnel test-section. To assess the extent of the dissolution related to the low DO_2 content. Nuclei populations were measured with DO_2 varied between 2 and 10 ppm for constant test section parameters ($p_t = 77$ kPa, $U_t = 7$ m/s, $\sigma_{gen} = 0.25$, and $\Delta p_{gen} = 400$ kPa). The measured concentration and distribution of bubbles are plotted in Fig. 14. A non-linear increase in total bubble concentration is observed with increasing DO_2, which is predominantly associated with an increase in the number of smaller bubbles. An approximate power law was again observed, the exponent of which increased with increasing DO2 content.

4.3 Tunnel operating parameters

The influence of the tunnel parameters on the injected bubble population is difficult to assess, as generator parameters cannot be kept fixed while independently varying the tunnel conditions. To gain some insights, one generator parameter was fixed, while the variation

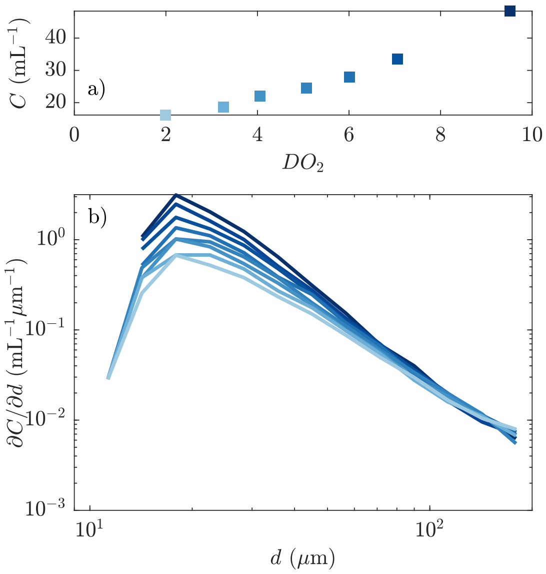

Fig. 14 a) Total bubble concentration (C) as a function of the dissolved gas level in the test section, for constant injector ($\sigma_{gen} = 0.25$ and $\Delta_{p_{gen}} = 400$ kPa) and tunnel parameters ($p_t = 77$ kPa and $U_t = 7$ m/s). Injector parameters are $\sigma_{\mathrm{gen}} = 0.25$ and $\Delta p_{\mathrm{gen}} = 400$ kPa. Test section parameters are $p_t = 77$ kPa and $U_t = 7$ m/s. The corresponding size distributions are plotted in b).

of the other was coupled to the matrix of prescribed tunnel conditions. Seven tunnel pressures, in the range between 20 kPa $\leq P_{\mathrm{t}} \leq$ 200 kPa, and five tunnel velocities , in the range between 3 m/s $\leq U_\infty \leq$ 11 m/s were tested. A map of total concentration across the complete range of tunnel conditions for a a fixed $\sigma_{gen} = 0.25$ is presented in Fig. 15a, and again for fixed $\Delta p_{gen} =$ 400 kPa in Fig. 15b. Contours of the unconstrained generator parameter are superimposed on the concentration map for reference. The empty triangle markers in Fig. 15b denote the data that was rejected due to visible presence of large millimeter size bubbles in the test-section, generated from gross audible cavitation in the generators operating at low σ_{gen}. In addition to this test matrix, measurements were made along the curve where the pressure in the plenum remained constant and the generators were operated with fixed $\sigma_{gen} = 0.25$ and $\Delta p_{gen} = 400$ kPa. The variation in dynamic pressure imposed by the changing test section velocity was compensated by changing the tunnel static pressure. These data, denoted by squares, are common to the two maps in Fig. 15.

For constant $\sigma_{gen} = 0.25$ bubble concentrations increased with an increase in tunnel velocity at the fixed tunnel pressure. The concentration also increased with tunnel pressure. The latter observation is in contrast with the expectation that higher tunnel pressure would aid bubble dissolution and result with a lower bubble concentration. However, an explanation for this behaviour can be found in the coupling of Δp_{gen} to the tunnel pressure, as the increase in the tunnel pressure results in the increasing driving pressure, and consequent increase in bubble production.

In the case where the driving pressure was held constant, the changes resulting from the variation in the tunnel parameters were masked by the more dominant effects of σ_{gen}. Strong similarity was observed in the concentration within a σ_{gen} contour band. An increase in bubble concentration was observed with increasing tunnel velocity and decreasing tunnel pressure. The variability in bubble concentration between the contours followed similar trends to those presented in Fig. 13a for the $\Delta p = 400$ kPa series (marked with circles). When operating correctly the generators produced a high concentration of bubble population until $\sigma_{gen} \approx 0.4$. The concentration transitioned between $0.4 < \sigma_{gen} \leq 0.5$ and diminished until very few bubbles for $\sigma_{gen} > 0.5$ were produced. These observations foster the premise that the changes in the measured bubble concentrations are, to a large extent, a result of variation in σ_{gen}.

In order to assess the effect of the tunnel operating conditions on bubble population in isolation of the generator parameters, the testing has to be performed with a fixed injected population. A fixed nuclei population can be generated by maintaining a constant plenum and saturation pressure (p_p,p_s) to produce constant Δp_{gen} and σ_{gen}. With this test the opposing effects of residence time and pressure on the bubble population evolution between the plenum and test-section can be examined. The tests were conducted for the test-section velocity varied between 2–13 m/s and a constant plenum pressure of 102 kPa. To account for the change in dynamic pressure with variable velocity, the test-section static pressure was varied between 20–100 kPa. The results for both the bubble total concentration and size distribution are presented in Fig. 16. In the absence of dissolution, it would be expected that the measured concentration would decrease six times as the flow velocity increases from 2 to 12 m/s, due to a fixed bubble population being injected for a higher water flow-rate. In addition, the dynamic pressure change between the plenum and the test-section should induce a growth in bubble size as the reduction in pressure between the plenum and test-section becomes larger as velocity increases. Neither of these changes are observed in the results, which indicates that the dissolution dominates the bubble population evolution as increasing pressure and longer residence times lead to a decrease in the total concentration. From the size distribution plot, it can be observed that the decrease in total bubble concentration is mostly associated with dissolution of the small bubbles due to their large surface to volume ratio. These process do not have a prominent effect on the concentration for bubbles larger than 50 µm.

These results are encouraging as together they show that the measured population in the tunnel is fairly insensitive to tunnel operating conditions. In general then, dense bubble populations can be produced for the majority of tunnel conditions by maintaining $0.15 < \sigma_{gen} < 0.3$ and a driving pressure $\Delta p \geq 300$ kPa. This produces bubble concentrations $C \approx 15-20$ mL^{-1}. For very low tunnel speeds and pressures, a reduced σ_{gen} is required to avoid gross cavitation in the generator outlet. Intermediate distributions are obtained by increasing the cavitation number of the generators until they reach the edge of their operational range. The critical σ_{gen} varies with the driving pressure Δp, a pseudo-measure for the generator Reynolds number. Operation in this range enables production of bubble concentrations $C = 0-15$ mL^{-1} where the distribution of bubble sizes changes slightly with tunnel conditions. Lower dissolved oxygen concentrations also reduces the number of bubbles observed in the test section.

5 Theoretical Dissolution

To contextualise the observed population, a quasi-steady model of bubble dynamics coupled with a diffusion model was applied to microbubbles of different sizes as they are advected from the injection point, through the tunnel contraction, to the test section entrance. Numerous models have been developed to account for the diffusion of gas between phases (Azbel, 1981), and studies such as Yu and Ceccio (1997) compare the congruence of select models to results obtained from experiments. Applicability of a model is usually assessed in terms of two limiting cases, with the understanding that most flows are a balanced combination of the two. In a stationary environment the problem is analogous to that of heat transfer in solid materials, where the 'film model' considers concentration gradients near the phase interface, and the related development of a diffusive boundary layer (Brennen, 2014). In turbulent flow the 'penetration model' considers the rate at which dissolved gas is convected from an interface by flow eddies (Azbel, 1981). Characterisation of the flow by Schmidt(Sc) and Sherwood(Sh) numbers aids in the selection and development of models. The majority of model validation has been performed on bubbles ~ 1 mm in diameter, using parameters such as the rise velocity to determine Sc and Sh numbers. The low Stokes number for bubbles on the order of micrometers in size makes determination of these values difficult and extrapolation of model results to microbubbles dubious. In addition, for the present work, Sc and Sh will vary as the level of turbulence changes between the location of bubble injection and the tunnel test section. Consequently, the film model (Brennen, 2014) was used to qualitatively discuss the effects of dissolution on the injected bubble population, where the magnitude of changes in bubble size with dissolution could vary.

As the flow approaches the tunnel test section, the change in the tunnel cross-sectional leads to an increase in the flow velocity and decrease in pressure. During this process bubbles are assumed to grow or shrink rapidly to permit a quasi-steady solution. The bubble radius due to pressure change has been modelled using

$$(p(t) - p_{\mathrm{v}})r^3 + 2\gamma r^2 - p_{G0}r_0^3 = 0, \tag{7}$$

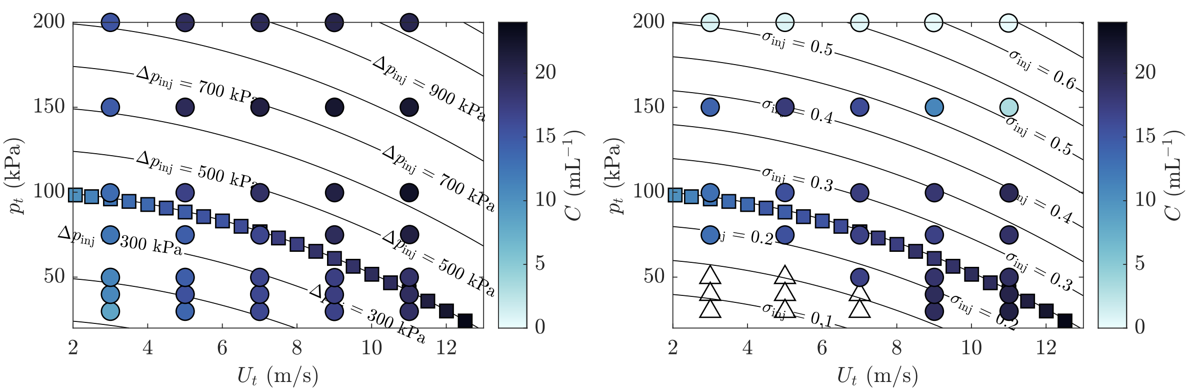

Fig. 15 Total bubble concentration as a function of test section velocity and pressure. In (a), the injector cavitation index is constant at 0.25, and the driving pressure is represented by the contour levels. In (b), the driving pressure is constant at 400 kPa. The injector cavitation number is given by the contour levels. Triangle points indicate where the injectors were suffering gross cavitation. The squares are the same data as Fig. ref and are all $\Delta p_{\mathrm{gen}} = 400$ kPa.

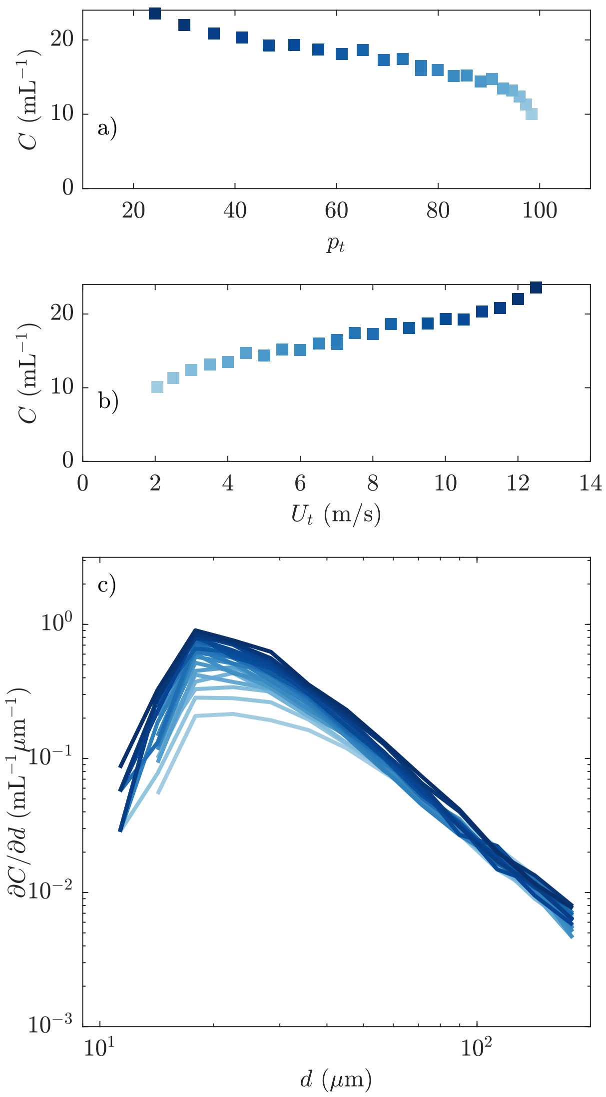

Fig. 16 Bubble concentrations presented for the case where the generator parameters, $\sigma_{gen} = 0.25$ and $\Delta_{p_{gen}} = 400$ kPa, and plenum pressure, $p_p = 102$ kPa, remained fixed while tunnel parameters vary. For the same data, total concentration is plotted against σ_t in a), and against U_t in b). The distributions for these data are shown in c).

for a bubble of radius r with initial radius r_0 and surface tension γ. The initial pressure of gas inside the bubble is p_{G0} , p_v vapour pressure, and $p(t)$ the pressure experienced by the bubble at time t. Together with the 'film model' for dissolution presented in Brennen (2014), a marching scheme for small dt is developed. Once the change in radius with external fluid pressure is calculated from 7, the gas pressure inside the bubble is calculated using

$$p_b = 2\frac{\gamma}{r} + p(t) - p_v. \tag{8}$$

Bubbles contain a mixture of gasses, but are mostly comprised of nitrogen and oxygen liberated upon condensation of vapour cavities. In the solution, oxygen constitutes approximately 20% of the dissolved gases. It is assumed that the injected bubbles are comprised of a similar mixture. Together with Henry's Law

$$c_s = \frac{P}{H}, \tag{9}$$

the concentration of a single gas species inside a bubble can be calculated from its partial pressure. In practice the various gasses will dissolve at different rates but for simplicity it has been assumed that oxygen is representative of the general dissolution process. Diffusive processes will usually grow a concentration boundary layer around the bubble (the 'film model') that may be stripped away by small scale turbulence, and relative motion between the bubble and the bulk flow (the 'penetration model'). As has been discussed, the determination of turbulence intensity and its effect on bubbles of this size is unclear. The model described in Brennen (2014) with a fully developed diffusive boundary layer was then applied to calculate the diffusive growth of a bubble in the given time step.

$$R = \sqrt{R_0^2 + \frac{2D(c_\infty - c_{sO_2})t}{\rho_g}}. \tag{10}$$

In Fig. 17a the ambient pressure history experienced by a bubble between the injection point and the test section entrance is plotted for the tunnel velocity $U_t =$ 7 m/s and the tunnel pressure $p_t = 78$ kPa. Bubbles spend the majority of their residence time in the slow moving plenum before being advected quickly through the contraction where the ambient pressure decreases by 20 kPa. In Fig. 17b the evolution of the bubble diameter calculated using the described model, with and without diffusion, and the pressure history from Fig. 17a has been plotted. The dissolved oxygen concentration was set to be $DO_2 = 30\%$ atmospheric saturation. Without diffusion a bubble 40 µm in size grows approximately 9% between the injection point and the test section. With diffusion, steady dissolution of the bubble causes it to shrink so that even after the pressure induced growth its size upon reaching the test section (d_t) is 5% lower than its original size (d_p). Dissolution occurs primarily during the extended residence in the plenum, with dynamic growth in the contraction occurring quickly at the end.

The balance of dissolution and dynamic growth depends on the bubble size and relative strength of surface

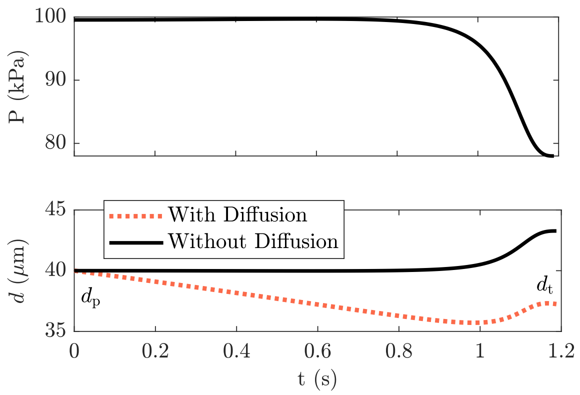

Fig. 17 a) The pressure history of a single bubble injected at the centerline of the tunnel is plotted as calculated from Bernoulli's equation upstream of the test section through the contraction for a tunnel speed U_t = 7 m/s, P_t = 78 kPa, $DO_2 = 30\%$ atmospheric saturation. b) The evolution of the bubble size under these conditions as modelled with and without the effects of diffusion.

tension during this process. The evolution of a range of bubble sizes using the model with the diffusion effect included, normalised by the bubble original size, is plotted in Fig. 18. Bubbles larger than 50 μm grow in size, while the increase in internal pressure due to surface tension caused bubbles ≤ 21 μm to completely dissolve.

The effect of tunnel conditions on the injected population is examined by using the theoretical model to calculate the bubble sizes upon reaching the test-section across the range of tunnel velocities and pressures. The ratio of the calculated and initial bubble size is then plotted against the initial bubble size. In Fig. 19 a plot denoting the effect of variation in the tunnel velocity in range between 2 and 12 m/s while the test section pressure is held constant is presented. Due to reduced residence time, the minimum bubble size at the injection point d_p required for a bubble to avoid being dissolved before the test-section, i.e. $d_t/d_p \geq 0$, decreases as the tunnel velocity is increased. For U_t = 2 m/s the pressure change through the contraction is so small that the effects of dissolution cause all bubbles to reduce in size. As the tunnel velocity increases the pressure change effect becomes increasingly dominant and at 12 m/s all but the smallest bubbles increase from their initial size.

For a fixed velocity of U_t = 7 m/s the tunnel pressure was varied from 10 to 200 kPa and the resulting effect on the bubble sizes is plotted in Fig. 20. Low test section pressures amplified bubble growth stemming from pressure change through the contraction. This was the result of increased tension applied to the bubbles as pressure in the tunnel approached their critical pressure. Decrease in the ambient pressure also re-

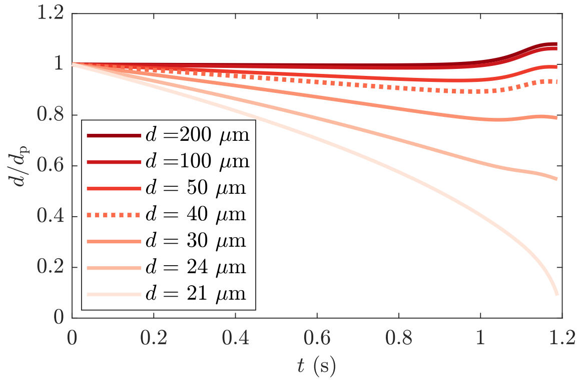

Fig. 18 Evolution of bubble size for the range of initial bubble diameters as they are advected towards the test section for U_t = 7 m/s, P_t = 78 kPa, DO_2 = 30% atmospheric saturation.

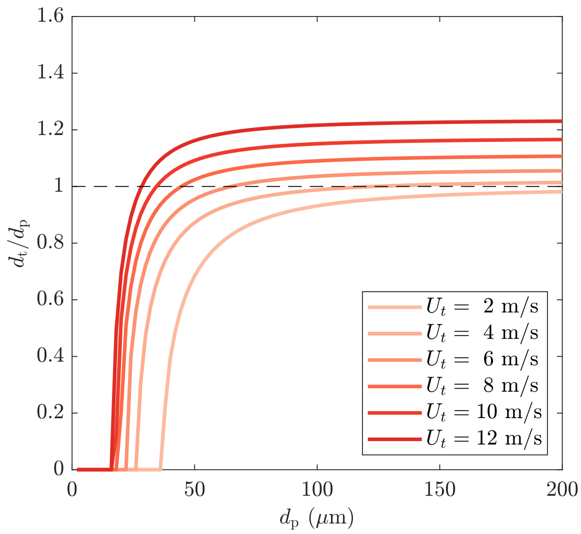

Fig. 19 The ratio of the final versus initial bubble size, across the range of initial bubble sizes, plotted for various tunnel velocities. The tunnel pressure is kept constant at P_t = 78 kPa, with dissolved oxygen concentration of DO_2 = 30% atmospheric saturation.

sulted in a decrease in the minimum bubble size that completely dissolved.

In experimental data, tunnel parameters could not independently varied without affecting generator parameters. A useful capability of the model is that it can be used to predict the effect of changing only one tunnel parameter for a set initial bubble population. The model was used to calculate a theoretical bubble population in the plenum from a bubble distribution measured in the test-section. This theoretical initial bubble population was then forward mapped to the test-section population while changing only one of the tunnel parameters. In Fig. 21 the simulated effect of changing tunnel pressure for a constant tunnel velocity is plot-

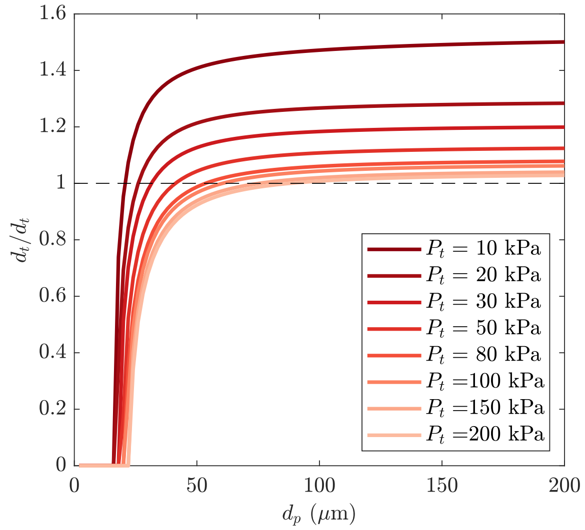

Fig. 20 The ratio of the final versus initial bubble size, across the range of initial bubble sizes, plotted for various tunnel pressures. The tunnel velocity is kept constant at U_t = 7 m/s, with dissolved oxygen concentration of DO_2 = 30% atmospheric saturation.

ted. In Fig. 22 the results of the same manipulation, but for changing tunnel velocity and constant pressure, are presented.

From Fig. 21 an increase in the concentration of larger bubbles can be seen as the pressure in the tunnel is reduced, while the concentration of small bubbles decreased. This is in contrast to the measurements presented in Fig. 16. The reason for this discrepancy stems from the model mapping principle. As the model functions by only mapping an initial bubble size to a final bubble size, the bubble size distribution curve can only be shifted and stretched along the horizontal axis, i.e. bubble diameter axis, while the curves remain unaffected along the concentration axis. In Fig. 22, it can be seen that the concentration of large bubbles increased following an increase in the tunnel velocity. The shift in size, in particular for small bubbles, is more pronounced at the lower tunnel velocities due to increased dissolution with extended residence time in the plenum.

There are two caveats to these simulated results. The first is that this modelling technique does not fundamentally alter the observed distribution, but rather maps the observed bubble size to a new diameter. It is then unable to capture non-linear change that is probabilistic in nature. For example, different bubbles within a population may experience random pressure histories imposed by the flow turbulence that would cause even a mono-disperse population to result in a distribution of resultant diameters. The second caveat, is that the consistent roll-off in concentration as the bubble size decreases below 15 µm might be artefact of optical measurement techniques at the edge of their dynamic range. It is possible that the power law like behaviour observed for larger sizes continues well below the lower limit of the MSI technique. The observed roll-off has been reported in numerous studies that utilise optical bubble/particle measurement (Liu et al., 1993; Russell et al., 2016; Mées et al., 2010). The fact that these mapped distributions do not concur with the measured data in Fig. 16 is therefore not surprising.

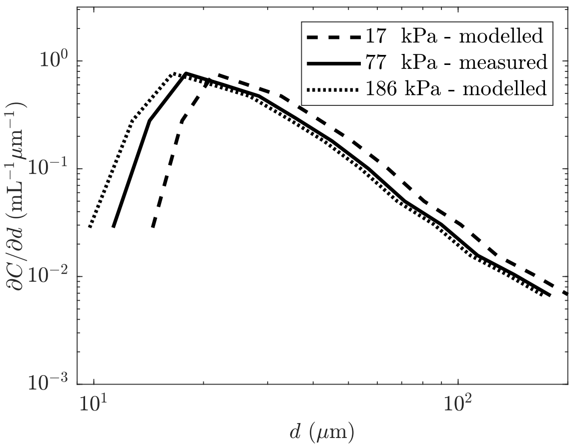

Fig. 21 A plot of modelled test-section populations for different tunnel pressures (p_t =17 and 186 kPa), obtained using backward mapping of the test-section population measured in the experiment (p_t = 77 kPa) to the plenum, and then forward mapped back to the test-section for different tunnel conditions. The experimental measurements were obtained for U_t = 7 m/s, σ_{gen} = 0.25 and $\Delta_{p_{gen}}$ = 400 kPa.

6 Conclusions

It has been demonstrated that injected nuclei populations can be measured for experiments in hydrodynamic test facilities with the MSI technique. Populations of 10–200 µm in diameter were measured with concentrations of 0–60 bubbles/mL. This system forms a vital component in the measurement of cavitation nuclei in hydrodynamic test facilities, capable of measuring semi-sparse bubble populations.

The acquisition and processing of microbubble measurements with MSI have a fast turn-around such that nuclei concentration measurements are approaching real-time. The method presented to calibrate the size dependent detection volume is of benefit as it is an *in-situ* calibration, which also extends the dynamic range of the technique. Estimation of the total bubble concentration

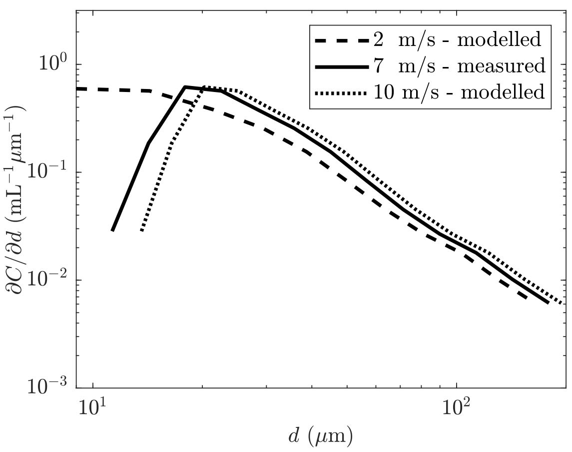

Fig. 22 A plot of modeled test-section populations for different tunnel velocities (U_t =2 and 10 m/s), obtained using backward mapping of the test-section population measured in the experiment (U_t = 7 m/s) to the plenum, and then forward mapped back to the test-section for different tunnel conditions. The experimental measurements were obtained for $p_t = 77$ kPa, $\sigma_{gen} = 0.25$ and $\Delta_{p_{gen}} = 400$ kPa.

was within 5% of the sampled concentration after only 100 bubbles were counted, but it was found that 10^4 detections were necessary for convergence of bubble size histograms. The large number of detections led the uncertainty in the total concentration measurements to be within 1%.

Tunnel velocity, pressure and dissolved oxygen concentration, as well as microbubble generator feed pressure (and hence saturation pressure) were varied, and the resultant concentration of bubbles measured in the test section. Low dissolved oxygen content in the tunnel led the measured population to decrease as they dissolved in the under-saturated environment between injection upstream and measurement in the test section. This dissolution is also a function of residence time so that the measured population increases with tunnel speed. Generator parameters are coupled to tunnel operating conditions through the pressure in the plenum where nuclei are injected. This produces a complex balance between bubble production and dissolution processes. Similar distributions are produced in high concentrations for low generator cavitation numbers. These distributions follow a power law suggesting that the generated populations also follow a power law. Intermediate concentrations are achieved at higher generator cavitation numbers, but exhibit a different distribution of bubble sizes. The critical cavitation number at which the generators begin to produce high concentrations increases with the driving pressure. It is reasoned that that this is an effect of increased generator Reynolds number but also the total gas content available to be liberated from the injected fluid. To decouple the microbubble production and dissolution processes and to develop a model for predicting the population in the test section, measurements of the population upstream in the plenum are required.

Acknowledgements This project was supported by the Australian Defence Science and Technology Group (Dr. Dev Ranmuthugala) through the 2017 U.S. Multidisciplinary University Research Initiative (Dr David Clarke), and the US Office of Naval Research (Dr. Ki-Han Kim, Program Officer) and ONR Global (Dr. Sung-Eun Kim) through NICOP S&T Grant no. N62909-15-1-2019. The authors are grateful for the technical assistance provided by Mr. Steven Kent and Mr. Robert Wrigley when conducting these experiments.

References

Albrecht HE, Damaschke N, Borys M, Tropea C (2013) Laser Doppler and phase Doppler measurement techniques. Springer Science & Business Media

Azbel D (1981) Two phase flows in chemical engineering. Cambridge University Press

Birvalski M, van Rijsbergen MX (2018) Application of interferometric particle imaging to cavitation nuclei measurements in a ship model basin. In: Proceedings of the 19th 2018 International Symposium on the Application of Laser and Imaging Techniques to Fluid Mechanics, Lisbon

Bohren CF, Huffman DR (2008) Absorption and scattering of light by small particles. John Wiley & Sons

Boucheron R, Aumelas V, Donnet M, Fréchou D, Poidatz A (2018) Comparative study of optical experimental methods for micro-bubble sizing. In: 19th International Symposium on Applications of Laser Techniques to Fluid mechanics, Lisbon, Portugal, p Paper 40

Brandner P, Lecoffre Y, Walker G (2007) Design considerations in the development of a modern cavitation tunnel. In: Australasian Fluid Mechanics Conference, pp 630–637

Brandner PA (2018) Microbubbles and Cavitation: Microscales to Macroscales. In: Proceedings of the 10th International Symposium on Cavitation (CAV2018), ASME Press

Brandner PA, Lecoffre Y, Walker GJ (2006) Development of an australian national facility for cavitation research. In: Sixth International Symposium on Cavitation, pp 1–9

Brennen CE (2014) Cavitation and bubble dynamics. Cambridge University Press

Brunel M, Shen H (2013) Design of ILIDS configurations for droplet characterization. Particuology 11(2):148–157, DOI https://doi.org/10.1016/j.partic.2012.06.014

Dehaeck S, van Beeck JPAJ (2007) Designing a maximum precision interferometric particle imaging setup. Experiments in Fluids 42(5):767–781, DOI 10.1007/s00348-007-0286-2

Doolan C, Brandner PA, Butler D, Pearce BW, Moreau D, Brooks L (2013) Hydroacoustic characterisation of the amc cavitation tunnel. In: Acoustics 2013 Victor Harbor: Science, Technology and Amenity, pp 1–7

Ebert E (2015) Optische messtechnik zur charakterisierung maritimer kavitationskeime. Thesis, Rostock University

Ebert E, Kröger W, Damaschke N (2015) Hydrodynamic nuclei concentration technique in cavitation research and comparison to phase-doppler measurements. Journal of Physics: Conference Series 656(1):012,111

Ebert E, Kleinwächter A, Kostbade R, Damaschke N (2016) HDNC - Nuclei size and number concentration estimation with detection volume correction. In: 31st Symposium on Naval Hydrodynamics, Monterey, California

Etter RJ, Cutbirth JM, Ceccio SL, Dowling DR, Perlin M (2005) High Reynolds number experimentation in the US Navy's William B Morgan large cavitation channel. Measurement Science and Technology 16(9):1701

Giosio D, Pearce B, Brandner P (2016) Influence of pressure on microbubble production rate in a confined turbulent jet. In: 20th Australasian Fluid Mechanics Conference (20AFMC), pp 1–4

Graßmann A, Peters F (2004) Size measurement of very small spherical particles by Mie Scattering Imaging (MSI). Particle & Particle Systems Characterization 21(5):379–389, DOI doi:10.1002/ppsc.200400894

Kawaguchi T, Maeda M (2005) Measurement technigure for analysis in two-phase flows involving distributed size of droplets and bubble sizing using interferometric method - planar simultaneous measurement of size and velocity vector field. Multiphase Science and Technology 17(1-2):57–77, DOI 10.1615/MultScienTechn.v17.i1-2.40

Khoo M, Venning J, Takahashi K, Ari J, Mori T, Pearce B, Brandner P, Ranmuthugala D (2017) Joint research between australia and japan on the cavitation inception of marine propellers and control surfaces. In: MAST Asia 2017, pp 1–6

Kobayashi T, Kawaguchi T, Maeda M (2000) Measurement of spray flow by an improved interferometric laser imaging droplet sizing (ILIDS) system. In: 10th International Symposium on the Application of Laser Techniques to Fluid Mechanics, Lisbon, Portugal, paper, vol 10

König G, Anders K, Frohn A (1986) A new light-scattering technique to measure the diameter of periodically generated moving droplets. Journal of aerosol science 17(2):157–167

Lacagnina G, Grizzi S, Falchi M, Di Felice F, Romano GP (2011) Simultaneous size and velocity measurements of cavitating microbubbles using interferometric laser imaging. Experiments in fluids 50(4):1153–1167

Lecoffre Y, Chantrel P, Teiller J (1987) Le Grand Tunnel Hydrodynamique (GTH): France's New Large Cavitation Tunnel for Hydrodynamics Research. In: International Symposium on Cavitation Research Facilities and Techniques, pp 13–18

Lindgren H (1966) Cavitation inception on head forms ittc comparative experiments. In: Swedish State Shipbuilding Experimental Tank, Göteborg, Sweden, Proceedings of the 11th International Towing Tank Conference, ITTC'66, Tokyo, Japan, Subject Performance, pp. 219-233. Paper: P1966-4 Proceedings.

Liu Z, Sato K, Brennen CE (1993) Cavitation nuclei population dynamics in a water tunnel. In: ASME, American Society of Mechanical Engineers, 153, pp 119–124

Masanobu M, Tatsuya K, Koichi H (2000) Novel interferometric measurement of size and velocity distributions of spherical particles in fluid flows. Measurement Science and Technology 11(12):L13

Mées L, Lebrun D, Allano D, Walle F, Lecoffre Y, Boucheron R, Fréchou D (2010) Development of interferometric techniques for nuclei size measurement in cavitation tunnel. In: Proceedings of the 28th Symposium on Naval Hydrodynamics

Mounaïm-Rousselle C, Pajot O (1999) Droplet sizing by mie scattering interferometry in a spark ignition engine. Particle & Particle Systems Characterization: Measurement and Description of Particle Properties and Behavior in Powders and Other Disperse Systems 16(4):160–168

Qieni L, Xiang W, Tong L, Zhen L, Yimo Z (2014) Linear interferometric image processing for analysis of a particle in a volume. Journal of Optics 16(4):045,703

Quérel A, Lemaitre P, Brunel M, Porcheron E, Gréhan G (2010) Real-time global interferometric laser imaging for the droplet sizing (ILIDS) algorithm for airborne research. Measurement Science and Technology 21(1):015,306

Russell PS, Giosio DR, Venning JA, Pearce BW, Brandner PA, Ceccio S (2016) Microbubble generation from condensation and turbulent breakup of sheet cavitation. In: 31st Symposium on Naval Hydrodynamics, Monterey, California

Russell PS, Venning JA, Brandner PA, Pearce BW, Giosio DR, Ceccio S (2018) Microbubble disperse flow about a lifting surface. In: 32nd Symposium of Naval Hydrodynamics, Hamburg Germany

Russell PS, Venning JA, Pearce BW, Brandner PA (2019) Calibration of Mie Scattering Imaging for microbubble measurement in hydrodynamic test facilities. Manuscript submitted for publication

Shen H, Coetmellec S, Brunel M (2013) Simultaneous 3D location and size measurement of spherical bubbles using cylindrical interferometric out-of-focus imaging. Journal of Quantitative Spectroscopy and Radiative Transfer 131:153–159, DOI https://doi.org/10.1016/j.jqsrt.2013.04.009

Skippon SM, Tagaki Y (1996) ILIDS measurements of the evaporation of fuel droplets during the intake and compression strokes in a firing lean burn engine. SAE transactions pp 1111–1126

Tropea C (2011) Optical particle characterization in flows. Annual Review of Fluid Mechanics 43:399–426

Weitendorf E, Friesch J, Song C (1987) Considerations for the New Hydrodynamics and Cavitation Tunnel (HYKAT) of the Hamburg Ship Model Basin (HSVA). In: Int'l. Symposium on Cavitation Research Facilities and Techniques, ASME, New York, NY

Yu P, Ceccio S (1997) Diffusion induced bubble populations downstream of a partial cavity. Journal of Fluids Engineering 119(4):782–787